33RD CONGRESS
OF THE INTERNATIONAL COUNCIL
OF THE AERONAUTICAL SCIENCES
STOCKHOLM, SWEDEN, 4-9 SEPTEMBER, 2022

ICAS 2022 SWEDEN

STUDY ON THE OBJECTIVE FUNCTION OF THE PROFILED ENDWALL OPTIMIZATION OF AN EMBEDDED COMPRESSOR STATOR

Jiayu Wang[1,*], Dejun Meng[1], Dongmin Feng[1], Qingwei Zhao[1]

[1] Shenyang Engine Research Institute of AECC, Shenyang, China

Abstract

This paper studied the endwall profiling in the embedded stator of a multistage compressor, with the method of numerical optimization based on CFD simulation and experimental test in multi-stage condition. A new objective function was constructed that combined the partial-blade-height parameters near the shroud endwall and the hub endwall. Compared with the traditional whole-blade-height parameter, the partial-blade-height parameter was more suitable to be the objective function at improving the endwall flow and reducing the blade loss coefficient, which can also reduce the optimization time. The numerical optimization results were verified in the multistage compressor test. The test of the secondary flow at the outlet the stator showed that the mechanism of the endwall profiling was that it reduced the local circumferential pressure gradient and circumferential secondary flow velocity, which can reduce the accumulation of low-energy fluid to the endwall region. This research promotes the application of endwall profiling technology in multistage compressor.

Keywords: profiled endwall optimization, objective function, partial-blade-height loss coefficient.

1. General Introduction

The design of aeroengine aims at high thrust weight ratio, which makes the pressure ratio of the compressor higher and higher [1-2]. The consequence is that the compressor is easier to drop into flow instability. In order to expand the stability margin of the compressor, lots of active control and passive control methods had been developed [3-5]. Among these methods, non-axisymmetric endwall profiling is a passive control method, and had been studied widely. The challenge of non-axisymmetric endwall profiling is to improve the compressor characteristic in the whole working range with the stability margin of the compressor not reduced [6-7].

At present, the research on the endwall profiling of compressor includes numerical simulation and experimental study. The research objects include linear cascade, single-row and single-stage compressor, but there is little research focusing on the multi-stage compressor environment [8-21]. The experimental study on compressor endwall profiling, especially the measurement of detailed flow field, only stays at the phase of cascade test [8,12,21]. Literature [9] introduced a CFD research on the application of endwall profiling in the multi-stage compressor environment. Firstly, an endwall profiling was designed in the single-row condition and then applied to each row of the multi-stage compressor directly, followed by a CFD simulation in the multi-stage environment. However, there was no experimental test on endwall profiling in the multi-stage condition.

The difficulty of the endwall profiling in the multistage compressor contains the following two aspects. From the perspective of CFD simulation, firstly, the simulation of multistage compressor is time-consuming, which makes the cost of optimization time unbearable. Secondly, the prediction ability of simulation on multistage is limited [22], which makes the design results are of great uncertainty that relying only on simulation [8-9]. From the perspective of experimental study, the experimental cycle of multi-stage compressor is longer, the cost is higher and the measurement is more difficult, compared with the test of linear cascade or single- stage compressor.

The technology of nonaxisymmetric endwall profiling has not been applied in military or civil compressors, which is caused by the lack of engineering experience in non-axisymmetric endwall optimization design in multi-stage compressor. Under this background, this paper takes the third stator of a four-stage axial compressor as the research object, the numerical optimization design and experimental research of the non-axisymmetric endwall in multi-stage compressor environment were carried out, which is of great significance for applying the non-axisymmetric endwall technology in multi-stage compressor to improve the endwall flow. It fills the blank of optimization design and experimental research of non-axisymmetric endwall technology in multistage axial compressor, and promotes the engineering application of this technology.

2. Research Object

The research was carried out in a four-stage low-speed axial compressor and the stator of the third stage (S3) was choose as the resarch object. The detailed structural parameters, test facilities and test results of the four-stage compressor were given in literature [23-24]. An optimization of profiled endwall had been done for S3 and an experimental study of S3 was carried out. The position of S3 and the test rig are shown in Figure 1.

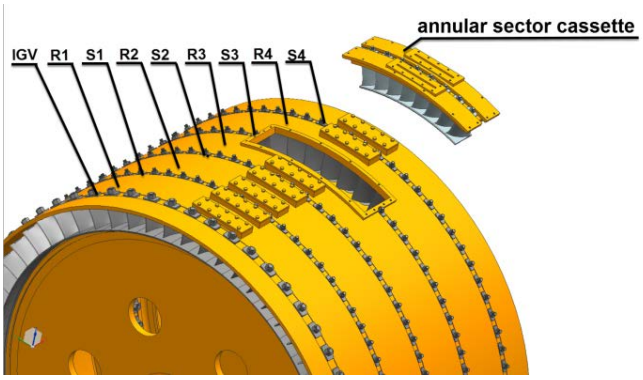

Figure 1 – Research object and the test rig

The inlet and outlet flow fields of the original stator at design point (DP) and near stall point (NS) are measured. The distribution of the normalized total pressure of S3 is shown in Figure 2, in which the normalized total pressure $\widetilde{p^*}$ is calculated by equation (1), where p^*, $\overline{p^*}$, $\overline{\rho}$ and U_{m} represent total pressure, average total pressure, average density and the rotating speed at midspan respectively.

$$\widetilde{p^*} = \frac{p^* - \overline{p^*}}{0.5 * \overline{\rho} * U_{\mathrm{m}}^2} \tag{1}$$

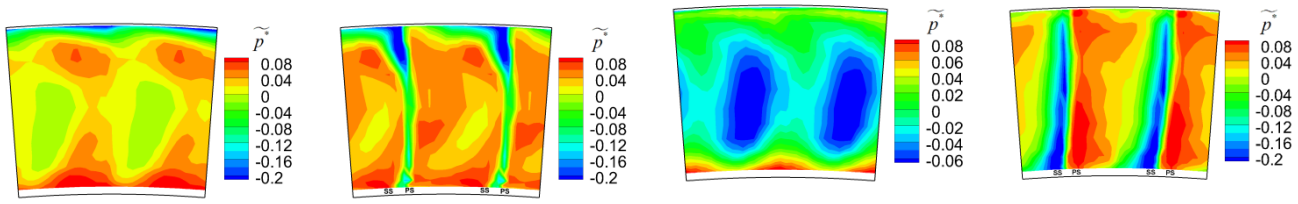

(a) S3 inlet at DP (b) S3 outlet at DP (c) S3 inlet at NS (d) S3 outlet at NS

Figure 2 – Normalized total pressure contour of S3 inlet and outlet (Test results)

According to the total pressure distribution at S3 outlet, the main flow defect at DP is the tip region, while the main flow defect at NS is the hub region. According to the flow defect positions at DP and NS, the positions for optimization design of endwall profiling are selected at both the shroud endwall and the hub endwall.

The total pressure loss coefficient (shorten as 'loss coefficient') of S3 is calculated by equation (2), where h, $\varpi(h)$, $p_{\mathrm{in}}^*(h)$, $p_{\mathrm{out}}^*(h)$ and $p_{\mathrm{in}}(h)$ represent the relative blade height, the radial distribution of loss coefficient, the inlet total pressure, the outlet total pressure and the inlet static

pressure. The distribution of loss coefficient of S3 at DP and NS are shown in Figure 3.

$$\varpi(h) = \frac{p_{\text{in}}^{*}(h) - p_{\text{out}}^{*}(h)}{p_{\text{in}}^{*}(h) - p_{\text{in}}(h)} \tag{2}$$

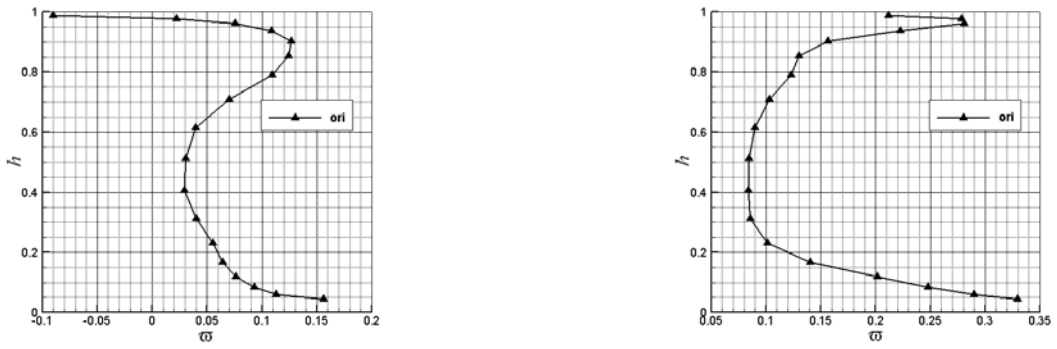

(a) DP (b) NS

Figure 3 – Loss coefficient of S3 (Test results)

Figure 3 (a) demonstrates that, the 90% span is the position of local maximum of the loss coefficient near the tip region, which corresponds to the center of the low-pressure region at S3 outlet in Figure 2 (b), while the loss coefficient at hub is large, which indicates that the flow at the hub region is poor as well. The loss coefficient near hub at NS is large, which corresponds to the flow separation at the hub region of S3 outlet in Figure 2 (d).

3. Optimization design platform

3.1 Optimization framework

The optimization design of endwall profiling is carried out on the Design3d module in the commercial software NUMECA. The flow chart of the whole optimization framwork is shown in Figure 4, which adopts the multi-objective optimization technology based on agent model.

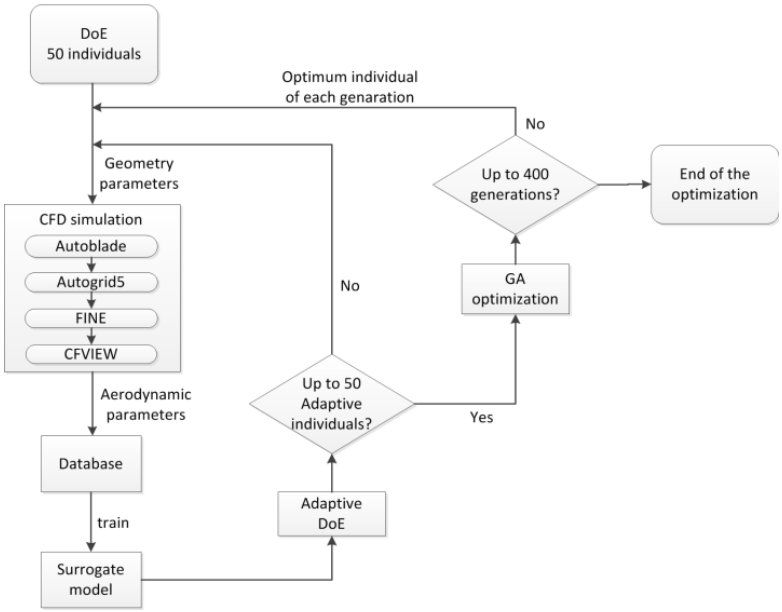

Figure 4 – Optimization framework

Firstly, an agent model is constructed by the radial basis function method. 50 individuals are selected from the design space by DOE (design of experiment) method. The selected individuals

are simulated by CFD simulation to build the initial sample database, which is used to train the agent model. Then 50 individuals are selected successively through the adaptive sampling method. The adaptive sampling method is to predict the performance of the whole design space according to the agent model. It samples in the region where the objective function is complex, and then the sample points are simulated through the CFD model. The results obtained by the CFD model are added to the database. With the continuous expansion of the database, the prediction accuracy of the agent model to the response parameters is getting higher and higher. Compared with the time-consuming CFD model, the agent model is time-saving. Each optimization step is driven by the genetic algorithm optimization based on the agent model. There are 400 steps in genetic optimization, each step includes 100 generations, and each generation includes 400 individuals, that is, 40,000 individuals are calculated in each step of optimization. These individuals are calculated through the agent model. The optimized individuals based on the agent model are then simulated by CFD simulation, and the CFD simulation results are added to the database. The agent model is continuously trained, and the updated agent model is used to the next step of genetic optimization. Continue this iteration until loop iterates reaches 400 steps of optimization.

3.2 CFD simulation chain

The CFD simulation chain constructs an accurate model compared with the agent model. It built a bridge from the design parameters (amplitude of disturbance point) to the response parameters (performance parameters). It includes endwall parametric modeling and flow field solution.

3.2.1 Parametric modeling of the endwall

The hub and shroud endwalls of S3 are parameterized in the Autoblade module of NUMECA. The distribution of the control points of the profiling surfaces are shown in Figure 5. 6 control points are evenly distributed along the circumferential direction and 8 control points along the axial direction. Each control point is given a disturbance amplitude along the radial direction. Limited by the size of the experimental facility, the disturbance amplitude of the shroud endwall is -6 mm to 6 mm and the disturbance amplitude of the hub endwall is -3 mm to 6 mm. The points at the same circumferential position or axial position are connected by B-spline curve respectively, so as to construct a smooth endwall surface. The axial boundary line of the endwall profiling should be consistent to maintain the periodic boundary. For each axial control line, the amplitude of the first and last points is 0, and the second and the last but one points are adjusted so as to ensure the slope of the first and last points are zero. Therefore, only four points in the middle are free variables. That is, there are 20 free variables for each endwall surface and 40 free variables for both endwall surfaces totally.

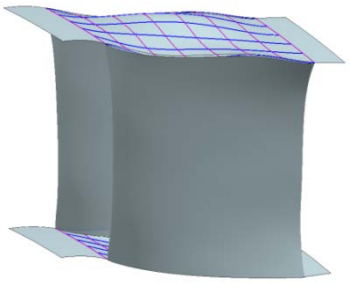

Figure 5 – Parametric modeling of the endwall

3.2.2 Flow field solution

The flow field solution is carried out in the FINE module of NUMECA. The computational domain is chosen to be the third stage. The inlet plane locates at 1 time of rotor chord length upstream the leading edge of the rotor, and the outlet plane locates at 1 time of stator chord length downstream the trailing edge of the stator. The inlet and outlet conditions of the computational domain are given by the total pressure, total temperature, velocity direction at inlet and the mass flow at outlet according to the experimental measurement results, which considered the boundary layer development of the front stage and the constraints of the rear stage. In this way, the flow environment of the third stage is constructed that reflects a four-stage condition.

It is assumed that the inlet conditions of the third stage remain unchanged during the optimization design of endwall profiling. The optimization mainly focuses on the influence to the flow field at S3 outlet and the corresponding loss coefficient of S3 during the optimization process of the endwall profiling.

3.3 Objective function

The objective function was constructed in the process of post-processing of flow field. In the optimization design of endwall profiling, the traditional objective function only pays attention to the overall parameters, such as pressure rise ratio, efficiency, total pressure loss coefficient, which reflect the change of aerodynamic parameters in the whole flow field. However, directly attention has not been paid to the detailed performance of flow, such as the loss coefficient near the endwall region. For the optimization of endwall profiling, its influence on the endwall region is more significant, but its influence to the overall performance parameters is limited. That is, it is difficult to capture the influence of endwall profiling through the changes of overall parameters. Many literatures [7-15] mentioned that after the optimization profiling of non-axisymmetric endwall, the distribution of loss coefficient of the row changes and the loss coefficient near endwall is significantly reduced. However, there is little research focuses on the optimization of partial loss coefficient near the endwall as the objective function.

The essence of how the non-axisymmetric endwall improve the flow condition of blade is that it changes the curvature of the flow near endwall through concave and convex modeling of the endwall geometry, and then improve the flow condition near the endwall. No matter how the endwall profiling impact the pressure gradient or the secondary flow intensity, these phenomenons occur near the endwall. If the objective function focuses on the loss coefficient of the whole-blade-height, it is obvious that the sensitivity to the endwall profiling will be reduced. According to this idea, the research team of this paper's author proposed a method for shroud profiled endwall optimization to an embedded stator with the strategy of partial-blade-height loss coefficient as the objective function and the optimization effects were experimentally confirmed in the multistage condition [24]. That paper only focus on DP and this paper furthermore focus on both DP and NS, as Figure 6 shows. Also, with the increase of state points, the profiling positions has been increased from the shroud endwall to both hub endwall and shroud endwall and the objective function changed from the loss coefficient near the shroud endwall to the combination of loss coefficient near the shroud endwall and near the hub endwall. The schematic diagram of whole-blade-height performance parameters and partial-blade-height performance parameters is shown in Figure 7.

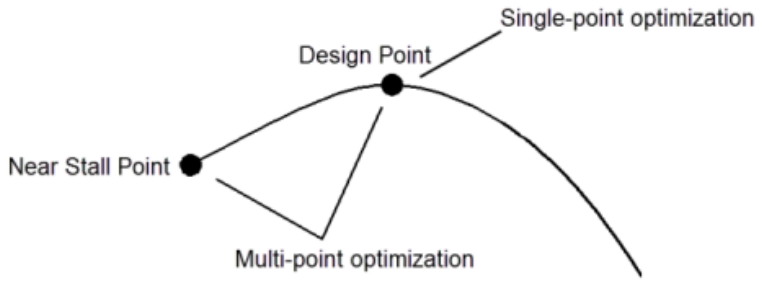

Figure 6 – Single-point optimization and multi-point optimization

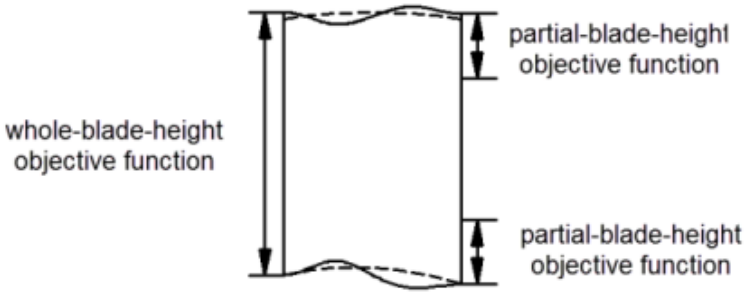

Figure 7 – Whole-blade-height performance parameter and partial-blade-height performance parameter

The optimization scheme with whole-blade-height and partial-blade-height loss coefficient as the objective function are shown in Table 1. All parameters are normalized with the CFD simulation results of the original S3. The first scheme is the traditional whole-blade-height loss coefficient as the objective function, represented by *W*. The second scheme is the partial-blade-height loss coefficient near the hub and shroud endwall proposed in this paper as the objective function, represented by *P*. In Table 1, *DP* in the subscript represents the design point and *NS* represents the near stall point, the subscript *o* in all denominators represents the loss coefficient of original S3. The subscript *w*, *h* and *t* stands for the whole blade height, near the hub region and near the tip region. In this paper, the near hub region takes from 0 to 0.1 span, and the tip region takes from 0.9 to 1 span.

Table 1 - Optimization scheme and the corresponding objective function

Optimization scheme	Objective function
W	$\varpi_W = \frac{1}{2}\left(\frac{\varpi_{DP,w}}{\varpi_{o,DP,w}} + \frac{\varpi_{NS,w}}{\varpi_{o,NS,w}}\right)$
P	$\varpi_P = \frac{1}{4}\left(\frac{\varpi_{DP,h}}{\varpi_{o,DP,h}} + \frac{\varpi_{DP,t}}{\varpi_{o,DP,t}} + \frac{\varpi_{NS,h}}{\varpi_{o,NS,h}} + \frac{\varpi_{NS,t}}{\varpi_{o,NS,t}}\right)$

4. Optimization design results

4.1 Endwall form

Figure 8 shows the optimization convergence history of two optimization schemes. It has been convergent after 400 steps of optimization. The optimized geometric forms of the endwalls obtained by each optimization scheme are shown in Figure 9, where Δr represents the radial difference between the magnitude of the optimized endwall geometry and the original S3, in mm. It can be seen that the profiling amplitude of scheme *P* is large than that of scheme *W*, whether in the shroud endwall or in the hub endwall.

(a) scheme *W* (b) scheme *P*

Figure 8 - Convergence history of the objective functions of each optimization scheme

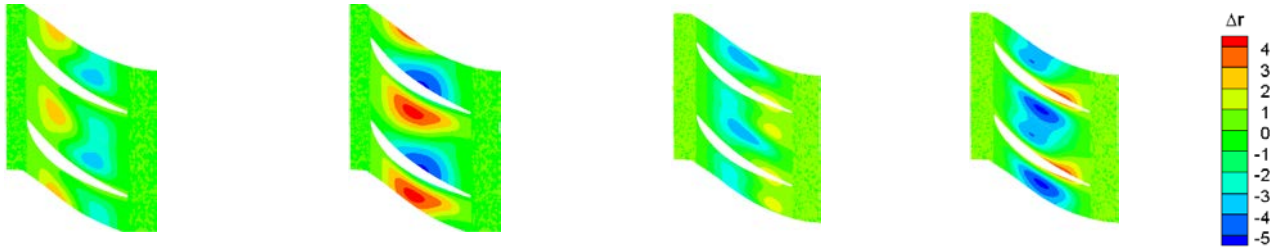

(a) scheme *W*, shroud (b) scheme *P*, shroud (c) scheme *W*, hub (d) scheme *P*, hub

Figure 9- Geometries of the optimized hub and shroud endwall of each optimization scheme

4.2 Loss coefficient

The radial distribution of the loss coefficient of the optimization results of scheme *W* and scheme *P* are shown in Figure 10. The reduction of the loss coefficient of scheme *W* and scheme *P* compared with original S3 is listed in Table 2.

As can be seen from Figure 10, the change of loss coefficient at DP is significantly lower than that at NS for both scheme *W* and scheme P. It can be seen from table 2 that through a limited number of steps (400 steps), not only the amplitude of the endwall of scheme *P* is larger than scheme *W*, but also the reduction of the loss coefficient of scheme *P* is greater than that of scheme *W* for both the loss coefficient of whole-blade-height and partial-blade-height. From the perspective of numerical simulation, it is proved that when the endwall profiling optimization design is carried out at both DP and NS, the optimization scheme focusing on the loss coefficient in the range of 10% blade height near the shroud and hub endwalls can effectively improve the flow condition of S3, which is better than the traditional optimization scheme focusing on the whole-blade-height loss coefficient.

(a) DP (b) NS

Fig.10 - Loss coefficients of S3 (CFD results)

Table 2 - Reduction of loss coefficients of scheme W and scheme P (CFD results, Unit: %)

scheme	*W*		*P*	
	DP	NS	DP	NS
ϖ_w	8.28	27.94	10.19	34.48
ϖ_h	8.12	24.71	13.17	29.41
ϖ_t	-12.56	15.95	15.23	28.62

4.3 Compressor characteristics

Since scheme *W* and scheme *P* are optimized in a single-stage environment, the influence of the optimization results on the characteristics of the four-stage compressor is numerical simulated. The simulation results are shown in Figure 11. When the flow coefficient is between 0.35 and 0.45, the

pressure rise coefficient and efficiency of scheme *P* are higher than those of scheme *W*. The flow of scheme *P* at the last state point is greater than that of scheme *W*, which makes the stability margin of scheme *P* lower than that of scheme *W*. At DP, the pressure rise coefficient of scheme *W* is increased by 2.17%, the efficiency is increased by 1.01%, the pressure rise coefficient of scheme *P* is increased by 2.27%, and the efficiency is increased by 1.04%. At NS, the pressure rise coefficient of scheme *W* increased by 2.02%, the efficiency increased by 3.13%, and the pressure rise coefficient of scheme *P* increased by 2.6%, the efficiency increased by 4.11%. Overall, the optimization effect of scheme *P* is better than that of scheme *W*.

(a) pressure rise characteristic (b) efficiency characteristic

Figure 11 - Contrast of the characteristics of the four stage compressor (CFD results)

5. Experimental research

Experimental research is carried out in the four-stage compressor environment for scheme *W* and scheme P. The inlet and outlet planes of S3 are measured in detail at DP and NS respectively.

5.1 Contour of total pressure at stator outlet

The normalized total pressure contour at S3 outlet is shown in Figure 12. Compared with the total pressure contour at S3 outlet at DP in Figure 12 (a,b) and Figure 2 (b), it can be seen that both scheme *W* and scheme *P* improve the flow in low-pressure region near the shroud, and the effect of scheme *P* is better. Compared with the total pressure contour at S3 outlet at NS in Figure 12 (c,d) and Figure 2 (d), for the low-pressure region at the hub, both scheme *W* and scheme *P* can inhibit the low-pressure region at the hub, and the effect of scheme *P* is better.

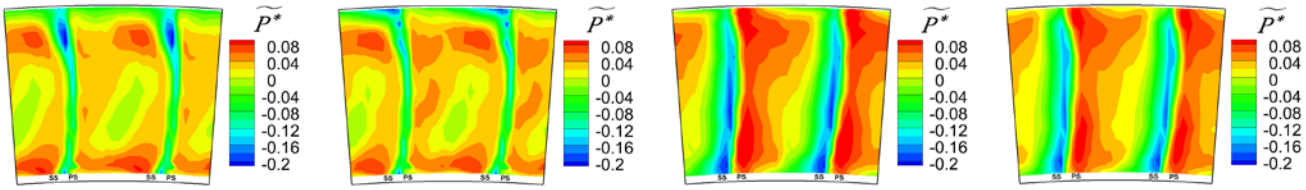

(a) Scheme *W* at DP (b) Scheme *P* at DP (c) Scheme *W* at NS (d) Scheme *P* at NS

Figure 12 – Normalized total pressure of S3 outlet (test results)

5.2 Loss coefficient

According to the experimental results of the inlet and outlet flow fields of S3, the loss coefficient of S3 for two optimization schemes is calculated and compared with that of S3. The results are shown in Figure 13 and table 3.

(a) DP (b) NS

Figure 13 - Loss coefficients of the original stator, scheme *W* and *P* at DP and NS (test results)

Table 3 - Reduction of loss coefficients of scheme *W* and *P* at DP and NS (test results) (Unit: %)

schemes	*W*		*P*	
	DP	NS	DP	NS
ϖ_w	8.09	2.32	12.76	6.88
ϖ_h	6.61	5.01	17.77	11.53
ϖ_t	20.66	1.83	40.47	20.09

At DP, it can be seen that both scheme *W* and scheme *P* reduce the loss coefficient of stator at full blade height, and the reduction of scheme *P* is greater than scheme *W*. At NS, the loss coefficient of scheme *W* is lower than that of scheme *P* at the position of 0.6 to 0.85 blade height, and the loss coefficient of scheme *W* at other blade height is greater than that of scheme *P*. The biggest difference between the simulation results and the experimental results is that the reduction of the loss coefficient of experimental result at NS is less than that predicted in the numerical simulation, which reflects the effect of multi-stage environmental and the necessity of experimental verification of the design results. Compared with the application of endwall profiling in linear cascade and single-rotor, single-stator or single-stage compressor, the interaction between the front and rear stages and the matching between stages in multistage compressor limit the experimental effect of endwall profiling. At NS, the flow environment in the compressor is the worst. The unsteady effect and the interaction effect between stages are quite strong. Therefore, it is difficult to completely and accurately predict NS characteristics in the multi-stage environment only through numerical simulation. Therefore, it is necessary to carry out experiments in the multi-stage compressor environment to verify the design results.

Through experimental research, it is proved that when the endwall profiling optimization design is carried out at DP and NS at the same time, the optimization scheme focusing on the loss coefficient in the range of 10% blade height near the shroud and hub endwall is better than the traditional optimization scheme focusing on the loss coefficient of whole-blade-height.

5.3 Secondary flow field at stator outlet

In order to study the change of endwall profiling on the secondary flow field at S3 outlet, the secondary flow velocity and flow field at S3 outlet are compared, and the circumferential secondary flow velocity $V_{\mathrm{t,sec}}$ and radial secondary flow velocity $V_{\mathrm{r,sec}}$ are defined as equation (3) and equation (4), where V_{t}, $\overline{V_{\mathrm{t}}}$, V_{r}, $\overline{V_{\mathrm{r}}}$ represent circumferential flow velocity, average circumferential flow velocity, radial flow velocity and average radial flow velocity respectively.

$$V_{\mathrm{t,sec}} = V_{\mathrm{t}} - \overline{V_{\mathrm{t}}} \tag{3}$$

$$V_{\mathrm{r,sec}} = V_{\mathrm{r}} - \overline{V_{\mathrm{r}}} \tag{4}$$

Figure 14 to Fig. 16 show the secondary flow contour and vector diagram for original S3, scheme *W* and scheme *P* respectively. Compared with the endwall profiling in the linear cascade, the secondary flow velocity change is less after the application of endwall profiling in the embedded stage, because the flow of the middle stage is restricted by the front and rear stages. Whether for DP or NS, the region with significant change of secondary flow velocity is mainly concentrated near the endwall region, and the change of circumferential secondary flow velocity is greater than that of radial secondary flow velocity, that means, the change of circumferential secondary flow velocity plays a leading role due to the endwall profiling

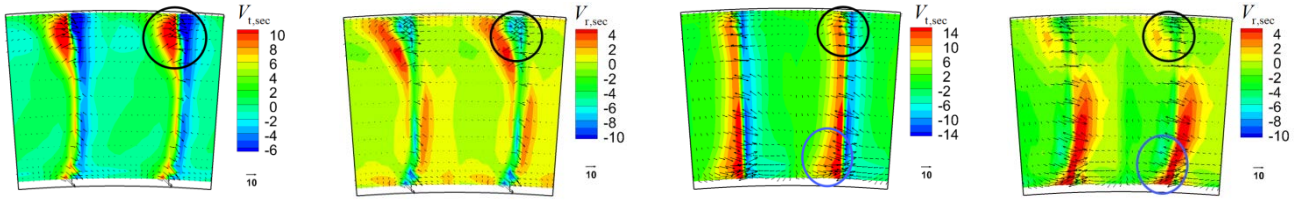

(a) Vt,sec at DP (b) Vr,sec at DP (c) Vt,sec at NS (d) Vr,sec at NS

Figure 14 – Secondary flow contour and vector diagram for protype S3

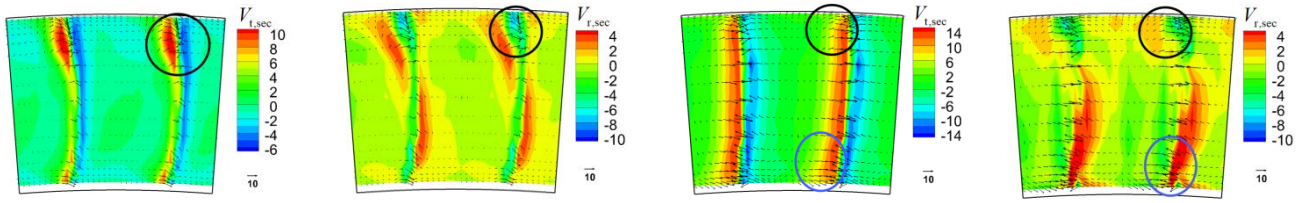

(a) Vt,sec at DP (b) Vr,sec at DP (c) Vt,sec at NS (d) Vr,sec at NS

Figure 15 – Secondary flow contour and vector diagram for scheme *W*

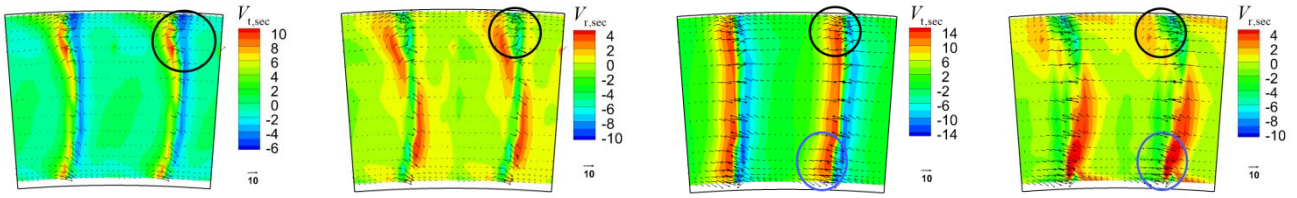

(a) Vt,sec at DP (b) Vr,sec at DP (c) Vt,sec at NS (d) Vr,sec at NS

Figure 16 – Secondary flow contour and vector diagram for scheme *P*

At DP, scheme *W* and scheme *P* significantly reduce the circumferential secondary flow velocity at the shroud region, and scheme *P* reduces the circumferential secondary flow to a greater extent. Due to the decrease of circumferential secondary flow velocity, the accumulation of low-energy fluid near the endwall from the pressure to the suction surface is reduced. The changes of circumferential secondary flow and radial secondary flow at the stator hub of scheme *W* and scheme *P* are not obvious. For DP, the reduction of loss coefficient at the hub is less than that at the tip.

For NS, the change of hub secondary flow velocity after optimization is greater than that of tip secondary flow velocity. At the hub of the stator, scheme *W* and scheme *P* reduce the circumferential secondary flow velocity, while the change of radial secondary flow is that the upward radial secondary flow velocity is more concentrated at the corner of the hub, so that the low-energy fluid at the hub/suction corner can transport the low-energy fluid to the mainstream radially.

There are two main understandings about the influence of non-axisymmetric endwall on the circumferential secondary flow velocity. The first is that the non-axisymmetric endwall reduces the local circumferential pressure gradient and circumferential secondary flow velocity [25,26], which can reduce the accumulation of low-energy fluid to the endwall region. The other is that the non-axisymmetric endwall increases the local circumferential pressure gradient and circumferential secondary flow velocity [8,27], which injects energy into the low-energy fluid in the corner region, These two understandings are inconsistent. Through the experimental study in multistage compressor in this paper, it is consistent with the first understanding that the non-axisymmetric endwall reduces the circumferential secondary flow velocity near the endwall region.

6. Conclusion

Through the optimization design of the third stage stator endwall in a four-stage compressor, this paper explores the optimization method of the non-axisymmetric endwall profiling of the embedded stator, and proves the reliability of this method through experimental research. The main

conclusions are as follows:

1. An optimization design method of non-axisymmetric endwall profiling of the embedded stator in a multistage compressor is developed, which is more time-saving and suitable for engineering, contrasting with the traditional endwall profiling method.

(a) The numerical simulation of the embedded stage is used as the optimization basis to optimize the shroud and hub endwalls of the embedded stator at DP and NS. The inlet conditions of the embedded stage in the simulation are from the outlet data of the front stage measured by the experiment, so that the endwall profiling optimization design based on the numerical simulation of the embedded stage can reflect the multi-stage compressor environment. Compared with the optimization based on the simulation of multi-stage compressor, optimization based on embedded stage is more time-saving.

(b) The objective function in the optimization is the partial blade height loss coefficient of 10% of the blade height near the shroud and hub endwall. Under few optimization steps (400 steps), the reduction of the whole-blade-height loss coefficient of the stator and partial-blade-height loss coefficient near endwall by this method is greater than that of the traditional whole-blade-height loss coefficient as the objective function.

By replacing the optimization based on multi-stage simulation with the optimization based on embedded stage simulation, and setting the objective function as the loss coefficient of partial blade height near the endwall, the endwall profiling optimization design in multi-stage compressor is realized, which greatly saves the optimization time and shortens the optimization design cycle, which lays a foundation for the engineering application of non-axisymmetric endwall technology in multi-stage compressor.

2. The secondary flow change after the non-axisymmetric endwall profiling of the embedded stator is studied experimentally. In the multistage compressor, due to the development of the boundary layer of the front stage endwall and the constraints of the rear stage, the optimization effect of the endwall profiling of the embedded stator is limited, so that the secondary flow velocity change at S3 outlet is lower than that of the non-axisymmetric endwall in the linear cascade or single-stage compressor. After the non-axisymmetric endwall stator profiling of the embedded stator, the secondary flow field at the stator outlet changes. The circumferential secondary flow velocity changes more, compared with the radial secondary flow velocity. After the endwall profiling, the circumferential secondary flow velocity near the endwall is reduced, and the accumulation of low-energy fluid from the pressure surface to the suction surface near the endwall is reduced, so as to improve the flow near the end region and reduce the total pressure loss coefficient in the end region.

7. Contact Author Email Address

The contact author email address is nuaawjy@126.com.

8. Copyright Statement

References

[1] LIU Qin, ZHOU Renzhi, WANG Zhanxue. Charac-teristic analysis on military aero-engines [J]. *Gas Turbine Experiment and Research*, 2014, 27(2):59-62.

[2] MENG Lingyong, GAO Haihong, ZHENG Tianhui, et al. Research on thrust-weight ratio of aero-engine [J]. *Gas Turbine Experiment and Research*, 2016, 29(2):57-62.

[3] STARK U, SAATHOFF H. Passive and active methods to enhance axial-flow compressor aerodynamics [C]. *Notes*

on Numerical Fluid Mechanics & Multidisciplinary Design. Heidelberg, Berlin: Springer, 2009: 145-167.

[4] D'Andrea R, Behnken R L, Murray R M. Active control of rotating stall using pulsed-air injection: a parametric study on a low-speed axial flow compressor [J]. *Sensing, Actuation, and Control in Aeropropulsion*, 1995, 2494: 152-165.

[5] Martin P, Wilson J, Berry J, et al. Passive control of compressible dynamic stall [R]. *AIAA 2008-7506*, 2008.

[6] Reising S, Schiffer H P. Non-axisymmetric end wall profiling in transonic compressors—Part I: Improving the static pressure recovery at off-design conditions by sequential hub and shroud end wall profiling [R]. *ASME GT2009-59133*, 2009.

[7] Reising S, Schiffer H P. Non-Axisymmetric End Wall Profiling in Transonic Compressors—Part II: Design study of a transonic compressor rotor using non-axisymmetric end walls—optimization strategies and performance [R]. *ASME GT2009-59134*, 2009.

[8] Harvey N W. Some effects of non-axisymmetric end wall profiling on axial flow compressor aerodynamics: Part I—Linear cascade investigation [R]. *ASME GT2008-50990*, 2008.

[9] Harvey N W, Offord T P. Some effects of non-axisymmetric end wall profiling on axial flow com-pressor aerodynamics: Part II—Multi-stage HPC CFD study [R]. *ASME GT2008-50991*, 2008.

[10] Li X, Chu W, Wu Y, et al. Effective end wall profiling rules for a highly loaded compressor cascade [J]. *Proceedings of the institution of mechanical engineers, Part A: Journal of Power and Energy*, 2016, 230(6): 535-553.

[11] Reutter O, Hemmert-Pottmann S, Hergt A, et al. Endwall contouring and fillet design for reducing losses and homogenizing the outflow of a compressor cascade [R]. *ASME GT2014-25277*, 2014.

[12] LIU X, JIN D, GUI X. Investigation of non-axisymmetric endwall contouring in a compressor cascade [J]. *Journal of Thermal Science*, 2017, 26(6): 490-504.

[13] CHEN Desheng, LIU Bo, NA Zhenzhe, et al. Optimized non-axisymmetric endwall contouring for axial compressor [J]. *Gas Turbine Experiment and Research*, 2013, 26(1): 16-21+52.

[14] GAO Xiang, CHAO Xiaoliang, JIA Yizhe. Numerical investigation on a transonic axia-flow compressor rotor with multi-objective endwall profiling optimization [J]. *Fluid Machinery*, 2017, 45(3): 26-32.

[15] Chu W, Li X, Wu Y, et al. Reduction of end wall loss in axial compressor by using non-axisymmetric profiled end wall: a new design approach based on end wall velocity modification [J]. *Aerospace Science and Technology*, 2016, 55: 76-91.

[16] WU Jichang, LU Xingen, ZHU Junqiang. Secondary flow analysis for non-axisymmetric endwall on the high-load compressor cascade [J]. *Journal of Aerospace Power*, 2011, 26(6): 1362-1369.

[17] CUI Ke, SONG Yanping, LIU Huaping, et al. Influence of bump end wall on cascade flow of high turningbowed compressor [J]. *Journal of Aerospace Pow*er, 2015, 30(5): 1236-1243.

[18] VARPE M K, PRADEEP A M. Non-axisymmetric endwall contouring in a compressor cascade with tip gap [R]. *ASME GT2014-26725*, 2014.

[19] LU Jialing, CHU Wuli, HU Shuzhen, et al. Application of endwall contour on subsonic axial flow compressor stage [J]. *Journal of Aerospace Power*, 2009, 24(5): 1101-1107.

[20] Lepot I, Mengistu T, Hiernaux S, et al. Highly loaded LPC blade and non axisymmetric hub profiling optimization for enhanced efficiency and stability [C]. *ASME 2001, GT2001-46261*.

[21] Hoeger M, Cardamone P, Fottner L. Influence of end-wall contouring on the transonic flow in a compressor blade [C]. *ASME 2002, GT-2002-30440*.

[22] LIU Baojie, ZHANG Shuai, YU Xianjun. Experimental and numerical calculation of a 4-stage repeating stage lowspeed simulation compressor [J]. *Aeroengine*. 2018, 44(5): 56-64.

[23] WANG J, HU J, JIANG C, et al. Design of a sector cascade applied in the middle stage of a compressor test rig [J]. *Journal of Thermal Science*, 2022, 31: 485- 494.

[24] WANG J, HU J, JIANG C, et al. Non-axisymmetric shroud profiled endwall optimization of an embedded stator and experimental investigation [J]. *Energies*, 2020, 13(3): 1-22.

[25] ROSE M G. Non-axisymmetric endwall profiling in the HP NGV's of an axial flow gas turbine [R]. *ASME 94-GT-249*, 1994.

[26] LI Qiushi, YANG Chun, XIAO Wenfu, et al. Numerical study on corner stall suppression by endwall modeling [J]. *Progress in Natural Science*, 2009, 19(5): 537-543.

[27] DENTON J D. Loss mechanisms in turbomachines [J]. *Journal of turbomachinary*. 1993, 115(4): 621- 656.